

On the nature of the *ISO*-selected sources in the ELAIS S2 region

F. Pozzi,^{1,2*} P. Ciliegi,² C. Gruppioni,^{2,3} C. Lari,⁴ P. Héraudeau,^{5,6} M. Mignoli,²
G. Zamorani,^{2,4} E. Calabrese,² S. Oliver⁷ and M. Rowan-Robinson⁸

¹*Dipartimento di Astronomia, Università di Bologna, via Ranzani 1, I-0127 Bologna, Italy*

²*INAF/Osservatorio Astronomico di Bologna, via Ranzani 1, I-40127 Bologna, Italy*

³*INAF/Osservatorio Astronomico di Padova, vicolo dell'Osservatorio 5, I-35122 Padova, Italy*

⁴*Istituto di Radioastronomia di Bologna, via Gobetti 101, I-40129 Bologna, Italy*

⁵*Max-Planck-Institut für Astronomie, Königstuhl 17, D-69117, Heidelberg, Germany*

⁶*Kapteyn Astronomical Institute, Landleven 12, 9747 AD Groningen, the Netherlands*

⁷*Astronomy Centre, CPES, University of Sussex, Falmer, Brighton BN1 9QJ*

⁸*Imperial College of Science, Technology and Medicine, Prince Consort Road, London SW7 2BZ*

Accepted 2003 May 12. Received 2003 May 8; in original form 2002 December 10

ABSTRACT

We have studied the optical, near-infrared and radio properties of a complete sample of 43 sources detected at 15 μm in one of the deeper ELAIS repeatedly observed regions. The extragalactic objects in this sample have 15- μm flux densities in the range of 0.4–10 mJy, where the source counts start diverging from no evolution models. About 90 per cent of the sources (39 out of 43) have optical counterparts brighter than $I = 21$ mag. Eight of these 39 sources have been identified with stars on the basis of imaging data; for another 22 sources, we have obtained optical spectroscopy, reaching a high identification percentage (30/43, ~ 70 per cent). All but one of the 28 sources with flux density > 0.7 mJy are identified. Most of the extragalactic objects are normal spiral or starburst galaxies at moderate redshift ($z_{\text{med}} \sim 0.2$); four objects are active galactic nuclei. We have used the 15- μm , $H\alpha$ and 1.4-GHz luminosities as indicators of star formation rate and we have compared the results obtained in these three bands. While 1.4-GHz and 15- μm estimates are in good agreement, showing that our galaxies are forming stars at a median rate of $\sim 40 M_{\odot} \text{ yr}^{-1}$, the raw $H\alpha$ -based estimates are a factor of ~ 5 –10 lower and need a mean correction of ~ 2 mag to be brought on the same scale as the other two indicators. A correction of ~ 2 mag is consistent with what suggested by the Balmer decrements $H\alpha/H\beta$ and by the optical colours. Moreover, it is intermediate between the correction found locally for normal spirals and the correction needed for high-luminosity 15- μm objects, suggesting that the average extinction suffered by galaxies increases with infrared luminosity.

Key words: galaxies: evolution – galaxies: ISM – galaxies: starburst – cosmology: observations – infrared: galaxies.

1 INTRODUCTION

Deep 15- μm galaxy source counts performed in recent years with several ISOCAM surveys have revealed a new population of faint sources, for which the observed source density is in large excess with respect to the Euclidean predictions. This evidence was first highlighted by the deep/ultradeep surveys (0.05–4 mJy), where at flux densities fainter than about 1 mJy the counts show a strong divergence from no-evolution models, with an increasing difference that reaches a factor of 10 around the faintest limits (0.05–0.1 mJy; Elbaz et al. 1999). Recently, the evidence of strong evolution has also been confirmed by the source counts derived in the S1 field of the

shallower European Large Area Survey (ELAIS; Oliver et al. 2000) through a new and independent data reduction technique (Gruppioni et al. 2002). These counts, based on a large number of extragalactic sources (~ 350) detected over a wide area (4 deg^2), sample with a high statistical significance the previously poorly covered flux density range between *IRAS* and the deep ISOCAM surveys (0.5–100 mJy). The ELAIS differential counts show a significant change in slope occurring around 2 mJy, from $\alpha \sim 2.35$ at brighter fluxes up to $\alpha \sim 3.6$ for fainter fluxes and down to the survey limits. This is in qualitative agreement with previous results, although the ELAIS counts are somewhat steeper and lower than the others at faint fluxes (see Gruppioni et al. 2002). Different authors have interpreted and modelled the observed 15- μm source counts (i.e. Xu 2000; Chary & Elbaz 2001; Franceschini et al. 2001; Rowan-Robinson 2001).

*E-mail: pozzi@bo.astro.it

Common to all the models is the assumption of strong evolution for dusty star formation in starburst galaxies.

In this context, the key instrument to put observational constraints on the proposed models and to study directly the nature of the sources responsible for the observed strong evolution is photometric and spectroscopic identification of sources at different 15- μm flux density levels. At faint fluxes, detailed identification studies have been published for three deep fields: the HDF-N, the HDF-S and the CFRS 1415+52 field. The three surveys reach the following limiting sensitivities at 15 μm : 220 μJy for the HDF-N and HDF-S (with a completeness of ~ 90 and ~ 30 –40 per cent, respectively, see Aussel et al. 1999; Oliver et al. 2002) and 350 μJy for the CFRS 1415+52 (with a completeness of ~ 100 per cent at this flux level, see Flores et al. 1999). Although now the HDF-N is >95 per cent spectroscopically complete (Franceschini et al. 2001; Elbaz et al. 2002), the only published data (Aussel et al. 1999) are relative to a subsample of 26 identifications out of a total 15- μm sample of 46 sources. In the shallower HDF-S survey, 13 out of 26 sources (50 per cent) have a spectroscopic redshift (Mann et al. 2002), while in the CFRS 1415+52 survey ~ 40 per cent (17/41) of the sources have a spectroscopic redshift (Flores et al. 1999). The median redshifts found are ~ 0.6 , ~ 0.5 and ~ 0.76 for HDF-N, HDF-S and CFRS 1415+52, respectively (the peak of the HDF-N distribution shifts towards $z \sim 0.7$ considering the redshift distribution of the larger sample discussed in Franceschini et al. 2001). The majority of the sources detected in the CFRS and HDF-S fields show ‘e(a)’ optical spectra (see Poggianti et al. 1999), typical of either post-starburst systems or active starburst galaxies obscured by dust. While Flores et al. (1999) support the first hypothesis, Rigopoulou et al. (2000), studying a subsample of high redshift HDF-S galaxies, favour the second hypothesis and conclude that the HDF-S sources are very powerful starburst galaxies hidden by a large amount of dust.

In this paper, we will present the first results of the identifications of 15- μm sources at intermediate flux density levels in the repeated S2 field of the ELAIS survey (Oliver et al. 2000). The S2 field is one of the smaller areas of the survey and data in this field have been reduced with the *LARI technique*, which was also used for the reduction of the main S1 Southern field (Lari et al. 2001, hereafter L01). Given its larger area and shallower depth with respect to the deeper fields, S2 is very well suited to providing useful information concerning the sources in an interesting flux density range (0.4–10 mJy). At these fluxes there is evidence of strong evolution in the starburst galaxy population.

The layout of the paper is as follows. In Section 2 we describe the 15- μm sample; in Section 3 we present the multiwavelength follow-up and the optical photometric identifications; in Section 4 we present the spectroscopic results, including spectral classification for the optical counterparts; in Section 5 we discuss the global properties of the 15- μm sources. In the last section we present our conclusions. We adopt $H_0 = 75 \text{ km s}^{-1} \text{ Mpc}^{-1}$, $\Omega_m = 0.3$ and $\Omega_\lambda = 0.7$ throughout the paper.

2 THE MID-INFRARED SAMPLE

The ELAIS survey (Oliver et al. 2000) is the largest survey performed with the *Infrared Space Observatory (ISO)* at 6.7, 15, 90 and 175 μm . In particular, the 15- μm survey (performed with the ISOCAM instrument) covers an area of $\sim 12 \text{ deg}^2$, divided into four main fields and several smaller areas. The S2 field is one of the smaller areas: centred at $\alpha(2000) = 05^{\text{h}} 02^{\text{m}} 24^{\text{s}}.5$, $\delta(2000) = -30^\circ 36'00''$, it consists of a single raster of $\sim 21 \times 21 \text{ arcmin}^2$ and covers

$\sim 441 \text{ arcmin}^2$. Since it has been observed four times, it is approximately a factor of 2 deeper than the main survey.

The 15- μm data have been reduced and analysed using the *LARI technique*, for which the application to the main field S1 has been described in detail in L01. Since S2 is a repeated field, the procedure of reduction has been the same as that used for the reduction of the central repeated part of S1 (S1.5), though the combined rasters in S2 are four instead of three. However, we have used an upgraded version of the software used for S1 improving the mapping procedure and the checks on individual sources (Lari et al. 2002; Vaccari et al., in preparation).

First, the reduction algorithm was applied to each of the four independent observations separately. For each observation, two maps were created, one for the signal and one for the noise. Sources were extracted separately in each field and a first cross-correlation with the optical charge-coupled device (CCD) catalogue in the *I* band was computed in order to put the four 15- μm observations on the same optical astrometric reference system. The four different observations were then combined and the sources extracted in the combined map (above the 5σ threshold). Finally, the source list was checked and the total fluxes computed through the procedure of ‘autosimulation’ described in L01.

In Fig. 1 the final map obtained for S2 is shown (typical rms is $\sim 13 \mu\text{Jy pixel}^{-1}$, somewhat better than the rms of $\sim 16 \mu\text{Jy pixel}^{-1}$, obtained in the S1.5 repeated field). Since the reduction method has been largely tested in the S1 field, in this work we have simulated only 40 sources of 1 mJy, to give an estimate of the completeness, of the flux scale and of the flux density and positions uncertainties. Almost all the injected sources are detected (37/40) at $\geq 5\sigma$. Thus, our sample is nearly complete (~ 93 per cent) at 1 mJy. At 0.7 mJy, we expect our sample to be >30 per cent complete. This was the completeness level found for the S1.5 field at the same flux level (repeated three times instead of four). The systematic flux bias found is 0.88 ± 0.04 (i.e. fluxes must be divided by 0.88, see L01); the fluxes were corrected by this factor. The flux errors have been computed by applying the relations found for S1.5 (see equation 3 of L01), by considering for each S2 source its rms, S/N ratio and

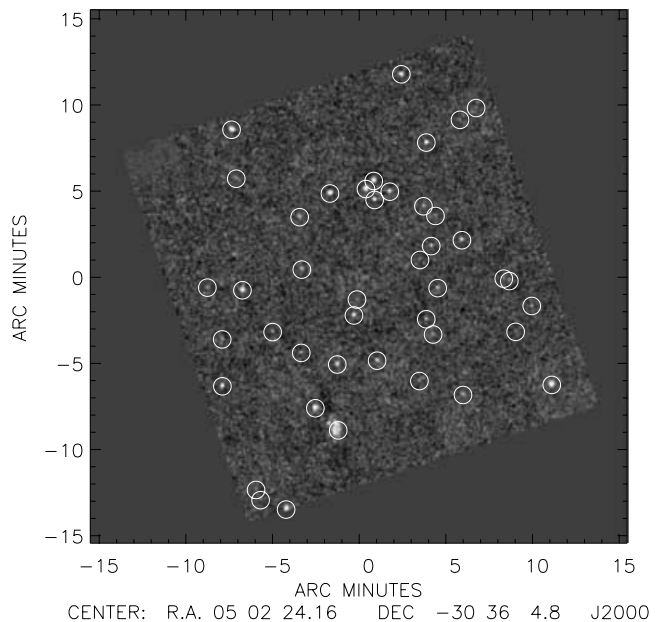


Figure 1. Grey-scale image of the S2 ELAIS field ($\sim 21 \times 21 \text{ arcmin}^2$). The circles indicate the location of all our detected sources (43 objects).

Table 1. The 15- μ m Catalogue in the ELAIS Southern Area S2.

<i>N</i>	Name	RA (J2000)	Dec. (J2000)	σ (RA) (arcsec)	σ (Dec.) (arcsec)	S_{peak} (mJy)	S/N ratio	S_{tot} (mJy)	σ (S_{tot}) (mJy)
1	ELAISC15_050143-303528	05 01 43.41	−30 35 28.18	1.2	1.1	0.080	6.17	0.523	0.087
2	ELAISC15_050147-303227	05 01 47.40	−30 32 27.91	1.2	1.1	0.079	6.78	0.484	0.074
3	ELAISC15_050147-302944	05 01 47.47	−30 29 44.26	0.8	0.6	0.600	45.75	3.446	0.382
4	ELAISC15_050149-304438	05 01 49.85	−30 44 38.81	0.8	0.7	0.684	37.44	4.177	0.466
5	ELAISC15_050151-304148	05 01 51.12	−30 41 48.06	1.2	1.1	0.091	6.90	0.602	0.094
6	ELAISC15_050152-303519	05 01 52.83	−30 35 19.20	0.8	0.6	0.582	40.82	3.567	0.397
7	ELAISC15_050156-302343	05 01 56.53	−30 23 43.00	1.3	1.2	0.076	5.53	0.472	0.081
8	ELAISC15_050157-302307	05 01 57.75	−30 23 07.47	1.3	1.2	0.107	5.70	0.712	0.124
9	ELAISC15_050200-303253	05 02 00.93	−30 32 53.52	0.9	1.0	0.155	11.77	0.921	0.115
10	ELAISC15_050204-302234	05 02 04.58	−30 22 34.81	0.8	0.7	0.831	30.08	6.255	0.712
11	ELAISC15_050208-303934	05 02 08.17	−30 39 34.19	0.9	1.0	0.187	11.38	1.094	0.137
12	ELAISC15_050208-303141	05 02 08.62	−30 31 41.09	1.0	1.0	0.134	9.67	0.788	0.103
13	ELAISC15_050208-303631	05 02 08.75	−30 36 31.45	1.0	1.0	0.153	10.73	0.948	0.122
14	ELAISC15_050212-302828	05 02 12.41	−30 28 28.07	0.8	0.6	0.698	53.11	4.610	0.511
15	ELAISC15_050216-304056	05 02 16.31	−30 40 56.89	0.8	0.6	0.790	67.43	4.782	0.528
16	ELAISC15_050218-303100	05 02 18.27	−30 31 00.55	0.9	0.9	0.180	13.77	1.105	0.134
17	ELAISC15_050218-302710	05 02 18.54	−30 27 10.93	1.0	1.0	0.136	9.99	0.815	0.106
18	ELAISC15_050222-303351	05 02 22.74	−30 33 51.58	0.8	0.7	0.366	28.10	1.926	0.216
19	ELAISC15_050223-303447	05 02 23.55	−30 34 47.08	1.2	1.1	0.082	6.25	0.491	0.077
20	ELAISC15_050225-304112	05 02 25.96	−30 41 12.39	0.8	0.6	0.653	49.29	4.040	0.448
21	ELAISC15_050228-304140	05 02 28.05	−30 41 40.47	0.8	0.7	0.464	36.45	2.900	0.324
22	ELAISC15_050228-304034	05 02 28.30	−30 40 34.24	0.8	0.8	0.319	23.60	1.971	0.225
23	ELAISC15_050228-303113	05 02 28.96	−30 31 13.99	0.8	0.9	0.215	16.09	1.358	0.162
24	ELAISC15_050232-304103	05 02 32.37	−30 41 03.17	0.8	0.7	0.321	25.03	1.858	0.210
25	ELAISC15_050235-304752	05 02 35.49	−30 47 52.37	0.8	0.8	0.348	19.00	2.127	0.247
26	ELAISC15_050240-303002	05 02 40.30	−30 30 02.96	1.2	1.1	0.079	6.01	0.564	0.099
27	ELAISC15_050240-303704	05 02 40.48	−30 37 04.98	1.3	1.2	0.076	5.05	0.486	0.089
28	ELAISC15_050241-304012	05 02 41.42	−30 40 12.24	1.0	1.0	0.125	9.32	0.822	0.113
29	ELAISC15_050242-303338	05 02 42.14	−30 33 38.29	1.0	1.0	0.126	9.19	0.773	0.104
30	ELAISC15_050242-304354	05 02 42.19	−30 43 54.35	0.8	0.8	0.320	23.82	2.164	0.249
31	ELAISC15_050243-303753	05 02 43.49	−30 37 53.32	1.0	1.0	0.119	9.71	0.666	0.086
32	ELAISC15_050243-303245	05 02 43.98	−30 32 45.11	1.2	1.1	0.096	7.04	0.620	0.095
33	ELAISC15_050244-303938	05 02 44.64	−30 39 38.43	1.3	1.2	0.075	5.56	0.509	0.091
34	ELAISC15_050245-303526	05 02 45.22	−30 35 26.80	1.1	1.1	0.101	7.63	0.797	0.130
35	ELAISC15_050251-304513	05 02 51.25	−30 45 13.44	1.3	1.2	0.069	5.28	0.447	0.081
36	ELAISC15_050251-303813	05 02 51.73	−30 38 13.71	0.8	0.8	0.252	19.35	1.705	0.200
37	ELAISC15_050251-302914	05 02 51.99	−30 29 14.25	1.2	1.1	0.078	6.35	0.531	0.088
38	ELAISC15_050255-304554	05 02 55.59	−30 45 54.50	1.3	1.2	0.070	5.09	0.394	0.067
39	ELAISC15_050302-303559	05 03 02.96	−30 35 59.59	1.3	1.2	0.072	5.21	0.444	0.078
40	ELAISC15_050304-303551	05 03 04.45	−30 35 51.09	1.2	1.1	0.093	6.57	0.732	0.129
41	ELAISC15_050306-303254	05 03 06.13	−30 32 54.05	1.3	1.2	0.066	5.35	0.432	0.078
42	ELAISC15_050310-303424	05 03 10.46	−30 34 24.25	1.1	1.1	0.111	8.33	0.708	0.100
43	ELAISC15_050315-302948	05 03 15.79	−30 29 48.89	0.8	0.6	1.603	115.82	10.275	1.132

Notes. Column 1: the *ISO* source number. Column 2: the source name. Columns 3 and 4: right ascension and declination at equinox J2000. Columns 5 and 6: the positional accuracy. Column 7: the source peak flux (in mJy pixel^{−1}). Column 8: the detection level (signal-to-noise ratio). Columns 9 and 10: the total flux (corrected for the flux bias) and its error (in mJy).

f_0 ('theoretical' peak flux, see L01). The positional error for each source is the combination of the uncertainties due to the reduction method (σ_{s+r}) and the uncertainties in the pointing accuracy (σ_p) (see equations 6 and 7 in L01). While for the reduction contribution we have assumed the expression found for S1_5, we have computed actual values for the pointing accuracy in S2 by cross-correlating the *ISO* sources with the *I*-band optical catalogue (see Section 3). Uncertainties in the pointing accuracy of about 0.2–0.3 arcsec have been obtained. These errors are negligible with respect to σ_{s+r} which is of the order of 1–2 arcsec, depending on the S/N ratio of each source.¹ A catalogue of 43 objects, with flux density in the range 0.4–10

mJy, has been obtained. The catalogue is presented in Table 1. The extragalactic source counts drawn from this catalogue are consistent with those obtained in S1_5 over the same flux density range (0.7–6 mJy).

3 MULTIBAND PHOTOMETRIC FOLLOW-UP

Optical follow-up has been obtained for the S2 field in the *U*, *B* and *I* bands with the WFI at the ESO 2.2-m Telescope. The optical catalogues are complete down to $U \sim 21.0$, $B \sim 24.5$ and $I \sim 22.0$

¹ The flux and positional errors computed following the above procedures must be considered as conservative estimates of the real uncertainties affect-

ing the S2 data (repeated four times), since the relations found S1_5 (repeated three times) have been used.

(Heraudeau et al., in preparation). Moreover, a near-infrared (near-IR) survey in the K' band has been obtained (over most of the S2 area) with SOFI at the ESO NTT, down to $K' \sim 18.75$ (Heraudeau et al., in preparation). The Automatic Plate Measuring (APM) catalogue (Maddox et al. 1990)² in the R band is also available down to $R_{63F} \sim 21$. Finally, the whole S2 area has been surveyed in the radio band at 1.4 GHz with the Australia Telescope Compact Array (ATCA) down to a 5σ flux limit of 0.13 mJy (Ciliegi et al., in preparation).

3.1 Optical and near-infrared identification of the ISO sources

We define the I -band catalogue as our master optical catalogue, which we used to search for the optical counterparts of the ISO sources using the likelihood ratio technique described by Sutherland & Saunders (1992). The likelihood ratio (LR) is the ratio between the probability that a given source at the observed position and with the measured magnitude is the true optical counterpart, and the probability that the same source is a chance background object. For each source we adopted an elliptical Gaussian distribution for the positional errors with the standard deviation in RA and Dec reported in Table 1 and assuming a value of 0.5 arcsec as the optical position uncertainty.

For each optical candidate we estimated also the reliability (Rel.), by taking into account, when necessary, the presence of other optical candidates for the same ISO source (Sutherland & Saunders 1992). Once the likelihood ratio has been calculated for all the optical candidates, one has to choose the best threshold value for LR (LR_{th}) to discriminate between spurious and real identifications. As the LR threshold we adopted $LR_{th} = 0.5$. With this value, all the optical counterparts of the ISOCAM sources with only one identification (the majority in our sample) and $LR > LR_{th}$ have a reliability greater than ~ 0.8 (we assumed a value of $Q = 0.9$ for the probability that an optical counterpart of the ISOCAM source is brighter than the magnitude limit of the optical catalogue, see Ciliegi et al. 2003, for more details). With this threshold value we find 39 ISO sources with a likely identification (four of which have two optical candidates with $LR_{th} > 0.5$). The same number of ISO/optical associations would be found using the less conservative value of $LR_{th} = 0.2$ (i.e. we do not have optical counterparts with $0.2 < LR < 0.5$). A summary of the results for the identification of the 43 ISO sources in the optical, near-infrared and radio bands is given in Table 2. As shown in column 4 of Table 2, all the likely optical counterparts lie within 4 arcsec from the ISO position, with the majority of them having an ISO–optical offset smaller than 2 arcsec.

The reliability of each optical identification is always very high (> 0.98 for 90 per cent of the sources), except for the four cases where more than one optical candidate with $LR_{th} > 0.5$ is present for the same ISO source. For these four sources we assumed that the object with the highest likelihood ratio value is the real counterpart of the ISO source. The number of expected real identifications (obtained by adding the reliability of all the objects with $LR_{th} > 0.5$) is about 38, i.e. we expect that ~ 1 of the 39 proposed ISO–optical associations may be spurious positional coincidences.

Starting from the I -band optical position of the 39 proposed ISO–optical associations we looked for U , B , R_{63F} and K' counterparts using a maximum distance of 1 arcsec (1.5 for the R_{63F} filter). For 10 of the 43 ISO sources K' -band data are not available (quoted as NA

in column 10 of Table 2). We found 31 (~ 72 per cent) counterparts in the U band, 37 (~ 86 per cent) counterparts in the B band, 32 (~ 74 per cent) counterparts in the R_{63F} band and 31 (~ 72 per cent) counterparts in the K' band. The same results are obtained using a search radius of 2 arcsec. The APM magnitudes of sources nos 4, 17, 25, 28 and 43 have not been reported since they appeared to be not reliable from a comparison with the magnitudes in the other bands. Three of these sources (nos 4, 17 and 25) are the brightest and more extended galaxies in our sample (see Fig. 5 in Section 4.3 for a 2×2 arcmin² map of source no 17), while sources nos 28 and 43 are stars of 12th and 11th magnitude, respectively.

Finally, for the four ISO sources without a likely optical counterpart in the I band (sources 19, 26, 38 and 39) we looked for possible counterparts in the U , B , R_{63F} , K' and radio bands using a maximum distance of 5 arcsec from the ISO position. However, no counterparts have been found for these four sources (see Section 5.1 for a discussion relative to these sources).

3.2 ISO radio associations

The radio catalogue in S2 consists of 75 1.4-GHz sources brighter than 0.13 mJy (5σ level). As a first step, a cross-correlation was performed between the radio catalogue and the 43 ISOCAM sources listed in Table 1. We find 13 reliable radio–ISO associations with a positional difference smaller than ~ 5 arcsec (except for the extended source no 17, where the centroids positions are at ~ 8.5 arcsec, see Fig. 5). Then, in correspondence with each ISOCAM position, we have searched for detection in the radio map down to a 3σ level (~ 0.08 mJy), finding eight additional radio identifications within 5 arcsec.

Assuming a 1.4-GHz source density of ~ 1000 sources deg⁻² at 0.08 mJy (Bondi et al. 2003), a maximum distance of 5 arcsec between the ISO and radio sources corresponds to a random association probability $[P = 1 - e^{-N(S)\pi d^2}]$, where $N(S)$ is the density of radio sources with flux greater than S and d is the distance between the ISO and the radio position] lower than 0.006. We therefore expect that essentially all of these radio sources are physically associated with the ISO sources.

Finally, we have verified that the positions of the radio and optical counterparts, associated with the same ISO source, are all consistent with each other.

4 SPECTROSCOPY

4.1 Observations

We have obtained spectroscopic data for 22 of the 39 likely optical counterparts. We did not observe eight objects with likely optical counterparts (sources nos 10, 15, 22, 28, 31, 33, 40 and 43) since they are easily classified as stars from the photometric data (see Fig. 4 in Section 4.3). All of them show, in fact, a clear stellar appearance and are characterized by a very bright I magnitude. Indeed, six of them have also been found in the stellar Tycho-2 catalogue (sources no 10, 15, 22, 28, 40 and 43, Hog et al. 2000).

The spectroscopic observations have been performed during 1999 December 5–6, using the ESO Faint Object Spectrograph and Camera Version 2 (EFOSC2) at the 3.6-m ESO Telescope. We used grism no 6, with spectral range 3860–8070 Å and a resolution of 4 Å pixel^{-1} (binning 2×2). The slit used was $1.2\text{--}1.5$ arcsec $\times 5$ arcmin. The exposure times varied from a minimum of 120 s for the brightest objects ($I \sim 14$ mag) up to a maximum of 2 h for the faintest objects ($I \sim 21$ mag) – to optimize the exposure time,

²The Automatic Plate Measuring machine is a National Astronomy Facility run by the Institute of Astronomy in Cambridge. See <http://www.ast.cam.ac.uk/~apmcat/>.

Table 2. Multiband properties and spectroscopic redshifts of the 15- μ m sources in the ELAIS S2 field.

<i>N</i>	<i>S</i> _{tot} (mJy)	<i>I</i>	Δ_I (arcsec)	LR	Rel.	<i>U</i>	<i>B</i>	<i>R</i> _{63F}	<i>K'</i>	<i>z</i>	$\Delta_{1.4\text{GHz}}$ (arcsec)	<i>S</i> _{1.4} ^{peak} (mJy beam ⁻¹)	<i>S</i> _{1.4} ^{tot} (mJy)
1	0.52	20.54	2.08	3.89	0.97	>21.00	>24.50	>21.00	17.15		1.59	0.11	0.09
2	0.48	17.70	1.87	45.04	0.99	19.72	19.66	18.29	15.56			<0.08	
3	3.45	17.18	0.87	183.72	0.99	19.21	18.86	17.46	15.03	0.127	0.95	0.48	0.38
4	4.18	14.15	0.77	241.89	0.99	16.52	16.07	–	12.28	0.050	1.59	0.43	0.43
5	0.60	19.88	1.06	24.09	0.99	>21.00	22.86	20.80	16.98		5.2	0.09	0.09
6	3.57	17.58	1.14	121.35	0.99	18.77	18.76	17.86	16.06	1.813		<0.08	
6		17.29	2.95	0.96	0.00								
7	0.47	19.66	2.85	2.96	0.75	>21.00	>24.50	>21.00	NA			<0.08	
7		15.71	3.98	0.84	0.21								
8	0.71	19.46	1.47	18.42	0.99	20.63	20.84	19.91	NA	0.600		<0.08	
9	0.92	17.83	1.72	51.55	0.99	20.18	20.06	18.40	15.41	0.308	0.84	0.21	0.26
10	6.26	10.54	0.92	4828.14	0.99	11.80	10.92	8.71	NA	0		<0.08	
11	1.09	20.64	1.06	12.75	0.99	>21.00	23.77	>21.00	17.75	0.627		<0.08	
12	0.79	17.16	3.83	0.53	0.84	18.54	18.69	17.40	15.19			<0.08	
13	0.95	19.25	1.51	19.15	0.99	>21.00	21.65	20.01	16.63	0.450	2.60	0.12	0.08
14	4.61	17.46	1.15	126.26	0.99	17.44	18.00	17.25	15.38	0.862	4.11	0.09	0.09
15	4.78	11.23	0.76	5128.13	0.99	14.45	13.48	9.98	9.82	0		<0.08	
16	1.11	18.60	1.31	45.65	0.99	20.90	20.39	19.56	15.94	0.128	2.01	0.14	0.14
17	5.6	12.52	0.01	554.57	0.99	15.07	14.00	–	10.51	0.020	8.50*	0.13	0.18
18	1.93	17.05	0.74	201.17	0.99	19.89	19.28	17.42	14.64	0.111	0.61	0.40	0.33
19	0.49	>22.00				>21.00	>24.50	>21.00	>18.75			<0.08	
20	4.04	17.56	0.07	289.72	0.99	20.72	20.04	18.17	14.91	0.191	2.17	0.69	0.87
21	2.90	16.86	0.63	218.17	0.99	19.40	19.18	17.43	14.56	0.191	0.87	0.33	0.45
22	1.97	11.13	0.99	3715.93	0.99	12.14	12.40	9.17	9.91	0		<0.08	
23	1.36	18.09	0.50	154.87	0.99	20.92	20.26	18.92	15.73	0.138	1.67	0.10	0.11
24	1.86	17.84	1.87	32.13	0.99	20.84	20.09	18.51	15.62	0.123	2.40	0.14	0.12
25	2.13	14.76	1.94	30.91	0.99	NA	16.10	–	NA	0.016	2.51	0.14	0.14
26	0.55	>22.00				>21.00	>24.50	>21.00	>18.75			<0.08	
27	0.49	18.25	4.00	1.02	0.91	>21.00	21.05	19.19	15.64			<0.08	
28	0.82	11.68	0.85	1749.25	0.99	12.41	12.80	–	10.46	0		<0.08	
29	0.77	17.12	0.89	128.63	0.99	19.56	19.08	17.31	15.04	0.125		<0.08	
30	2.16	17.71	0.61	204.91	0.99	20.81	20.05	18.29	15.17	0.170	2.11	0.41	0.42
31	0.67	12.14	1.70	437.34	0.99	14.27	13.78	11.43	10.39	0		<0.08	
32	0.62	20.39	2.49	3.27	0.97	>21.00	23.57	>21.00	17.07		2.61	0.10	0.10
33	0.51	12.82	2.42	73.83	0.99	15.63	14.46	12.41	11.18	0		<0.08	
34	0.80	19.39	2.52	4.56	0.72								
34		20.70	2.57	1.66	0.26	>21.00	>24.50	>21.00	17.98	0.775	3.00	0.33	0.54
35	0.45	20.61	1.87	5.01	0.98	21.82	22.37	>21.00	18.59			<0.08	
36	1.71	16.92	0.81	166.70	0.99	18.89	18.73	17.14	14.81	0.150	2.45	0.17	0.31
37	0.53	18.65	2.71	6.82	0.67	20.20	20.19	19.41	16.43	0.279	1.68	0.16	0.13
37		20.54	2.23	3.16	0.31								
38	0.39	>22.00				>21.00	>24.50	>21.00	NA			<0.08	
39	0.44	>22.00				>21.00	>24.50	>21.00	NA			<0.08	
40	0.73	11.41	0.94	2699.30	0.99	12.70	12.68	10.32	NA	0		<0.08	
41	0.43	18.55	0.57	55.74	0.99	20.54	20.36	19.31	NA			<0.08	
42	0.71	17.89	0.69	132.31	0.99	19.38	19.38	18.47	NA	0.172	1.75	0.10	0.16
43	10.28	9.83	3.21	3.86	0.97	10.9	11.10	–	NA	0		<0.08	

Notes. Column 1: the *ISO* source number. Column 2: the 15- μ m total flux (in mJy). Column 3: the *I*-band magnitude of the optical counterpart. Columns 4–6: the offset (in arcsec) between the *ISO* position and the optical counterpart in the *I* band, its likelihood ratio LR and reliability rel. Columns 7–10: the magnitude in the *U*, *B*, *R*_{63F} and *K'* bands. The (–) symbol in column 9 indicates an unreliable APM magnitude. NA in column 10 indicates that the *K'* magnitude is not available. Column 11: the spectroscopic redshift (see Section 4.1). Columns 12–14: the distance (in arcsec) between the *ISO* and the radio counterpart, the 1.4-GHz peak and total fluxes of the radio counterpart. The (*) symbol for object no 17 indicates a large distance between the *ISO* and radio centroids (see Fig. 5).

when possible two objects have been observed simultaneously by rotating the slit.

4.2 Data reduction

The data reduction has been performed using IRAF and the add-on package RVSAO, which contains tasks to obtain radial velocities from

spectra using cross-correlation and emission-line fitting techniques. To remove the pre-flash illumination, for each night a median bias (obtained from a sample of ‘zero exposures’ taken at the beginning and at the end of the night) has been subtracted from all the frames. To remove the pixel-to-pixel variations, the frames have been calibrated using flat-fields obtained from an internal quartz halogen lamp located in the dome. To calculate and subtract the background,

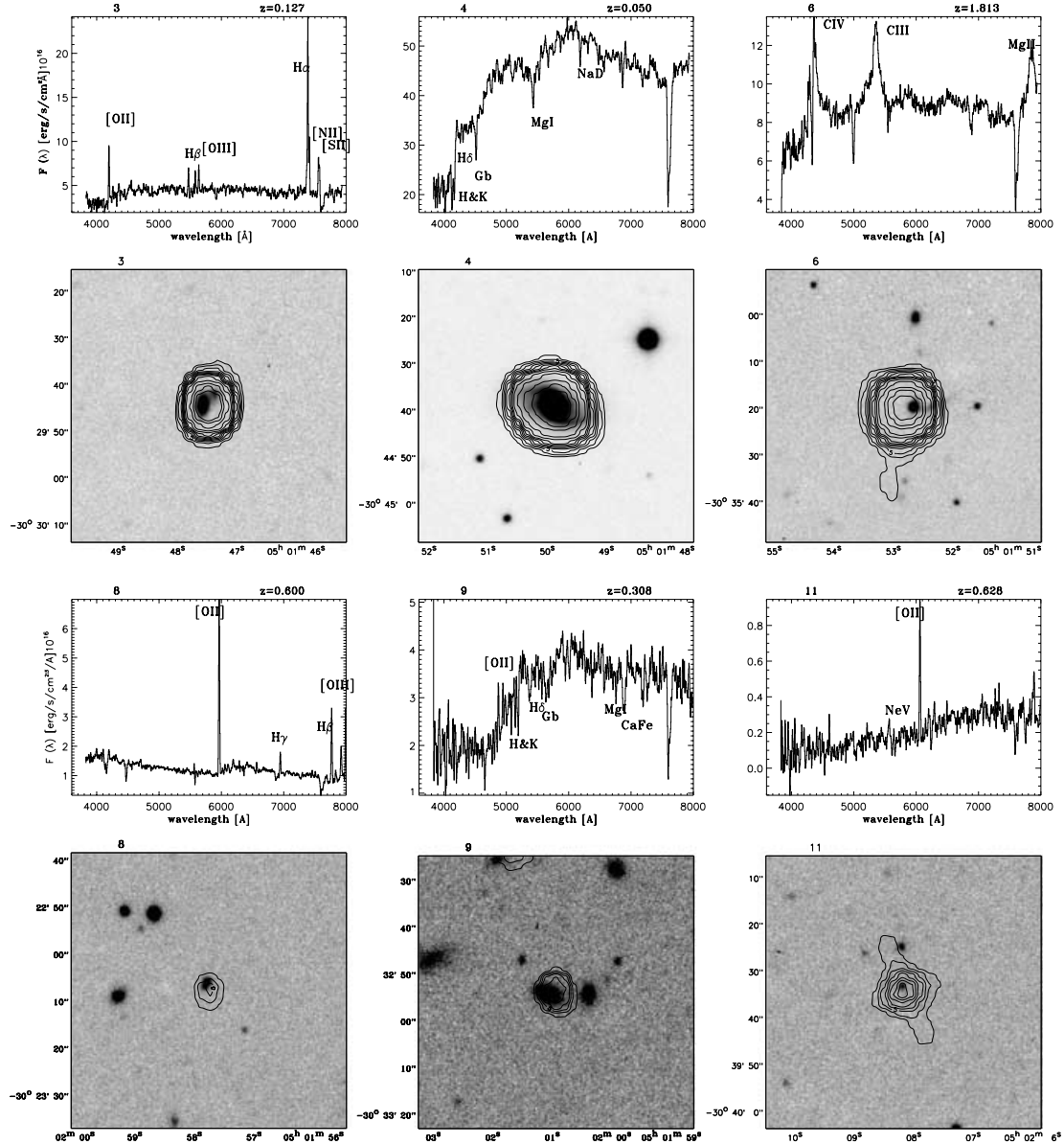


Figure 2. EFOC2 spectra of 21 of the 22 spectroscopically identified extragalactic objects with their corresponding *I*-band CCD images (data for source no 17 are shown separately in Fig. 5). The size of each image is 1×1 arcmin². Contour levels of the 15- μ m emission corresponding to [3, 4, 5, 6, 7, 8, 9, 10, 12, 15, 20, 25, 30, 50, 100] σ are superimposed on each optical image.

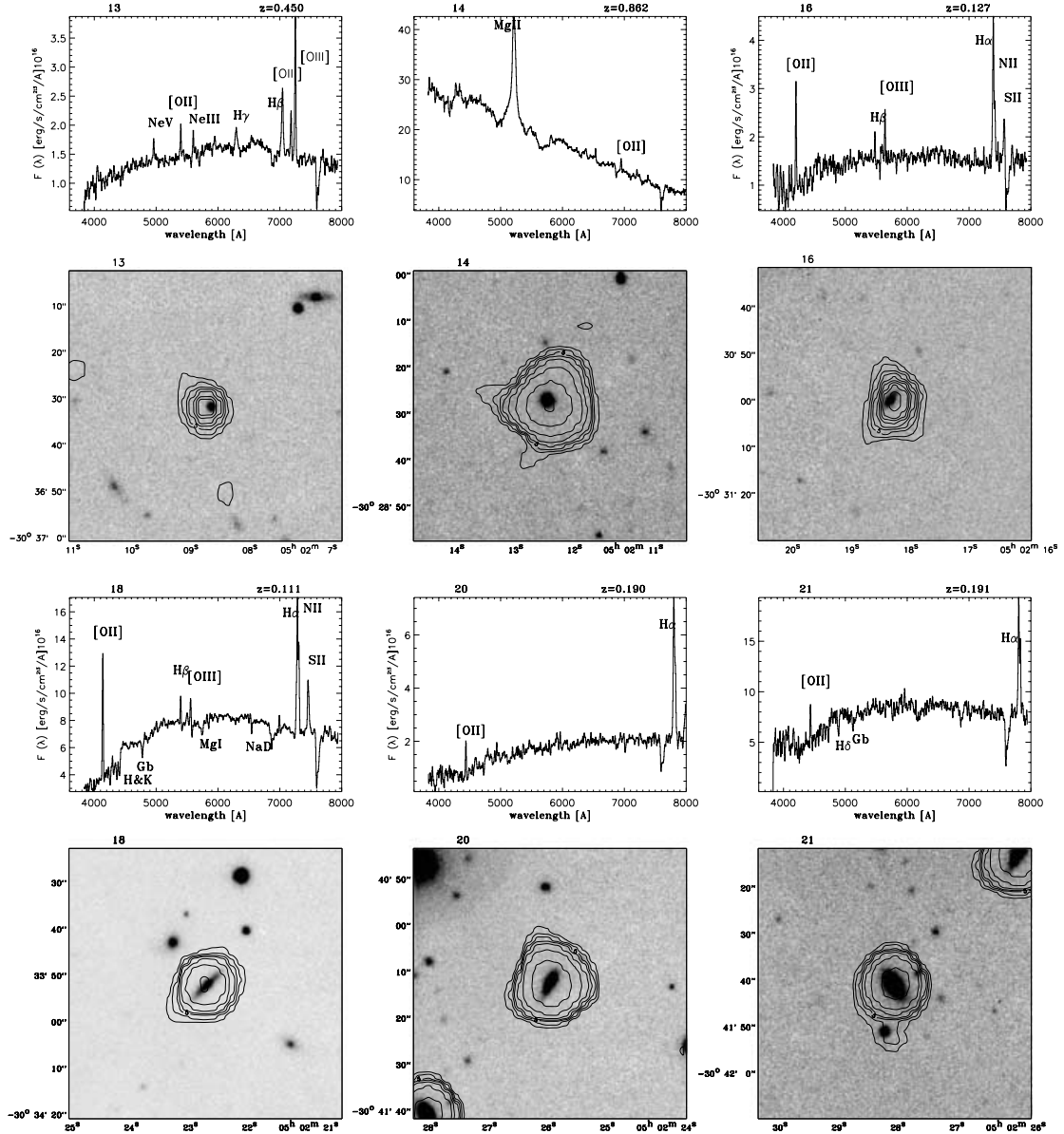
a fit has been performed to the intensity along the spatial direction in the columns adjacent to the target position. The spectrum for each galaxy was extracted using the *APEXTRACT* package. Standard wavelength calibration was carried out using helium–argon lamp exposures, taken at the beginning and the end of each night. Finally, to calibrate the flux, three standard stars have been observed each night (LTT 1020, LTT 377 and LTT 3218; Hamuy et al. 1992, 1994). Since several objects have been observed in more than one exposure (to keep the single integration times shorter than 1200 s) spectra associated with the same object have been combined together to obtain a better S/N ratio.

4.3 Optical spectra and classification

From our spectroscopic observations and reduction we were able to obtain a reliable redshift determination for all the observed sources

(22 objects), reaching a high identification percentage (30/43, ~ 70 per cent), also considering the eight stars. Moreover, all but one of the 28 sources with flux density >0.7 mJy are identified (see Fig. 6 in Section 5.1). In Fig. 2, 21 spectra are presented, together with the corresponding *I*-band images with superimposed contour levels of the 15- μ m emission. Source no 17 is presented separately in Fig. 5, because of its extension. The optical images shown in Fig. 3 correspond to the non-stellar sources (13 objects) without spectral information; Fig. 4 shows the optical images of the stellar sources (eight objects).

Redshifts have been determined by Gaussian-fitting of the emission lines and via cross-correlation with template spectra for the absorption-line cases. As templates for the cross-correlation we used those of Kinney et al. (1996). The results of the analysis are presented in Table 3. The line equivalent width (EW) and the $H\alpha$ fluxes reported in Table 3 have been measured using the package *SPLOT*

Figure 2 – *continued*

within the IRAF environment, comparing the results found with a Gaussian fitting and interactively choosing the endpoints. Repeated measurements show that the typical uncertainty in the EW is a few per cent for the strongest lines, but can be as high as ~ 30 – 40 per cent for the weakest lines. We were able to separate the $H\alpha$ line from the $[N II]$ line for the majority of our sources. When this was not possible, the EW and flux of $H\alpha + [N II]$ have been measured, estimating the EW and flux of $H\alpha$ by assuming an average ratio $[N II]/H\alpha \approx 0.5$ as found by Kennicutt (1992). The assumed value of 0.5 is consistent with our data; in fact, from the six sources with deblended $H\alpha$ and $[N II]$ we obtain 0.47 ± 0.03 (these cases have been highlighted in Table 3).

We have classified the objects as galaxies, active galactic nuclei (AGN) (type 1 and 2) and stars (last column of Table 3). We have first tried to subdivide the galaxy class into different categories according to Poggianti & Wu (2000, hereafter PW00). This classification is mainly based on two lines ($[O II]$ in emission and $H\delta$ in absorption) and is more appropriate for investigating the star formation proper-

ties of galaxies since these two lines are good indicators of current and recent star formation episodes, respectively. However, given the limited resolution of our spectra (especially critical for the weakest lines such as $H\delta$), in the end we used a coarser classification and divided our galaxies into three categories:

- (i) early-type galaxies – elliptical-like spectrum with little ongoing or recent star formation;
- (ii) normal spiral galaxies – with $H\alpha$ or $[O II]$ present [$EW([O II]) \leq 40 \text{ \AA}$]; this category includes both the $e(a)$ and the $e(c)$ galaxies of PW00;
- (iii) starburst galaxies – with very strong emission lines [$EW([O II]) \geq 40 \text{ \AA}$]; this category corresponds to the $e(b)$ class of PW00.

The dominant class ($16/22 \sim 73$ per cent) of the extragalactic sources is comprised of galaxies characterized by star formation at different levels. AGN (type 1 and 2) constitute ~ 18 per cent ($4/22$) of the sample and early-type galaxies constitute ~ 9 per cent of the

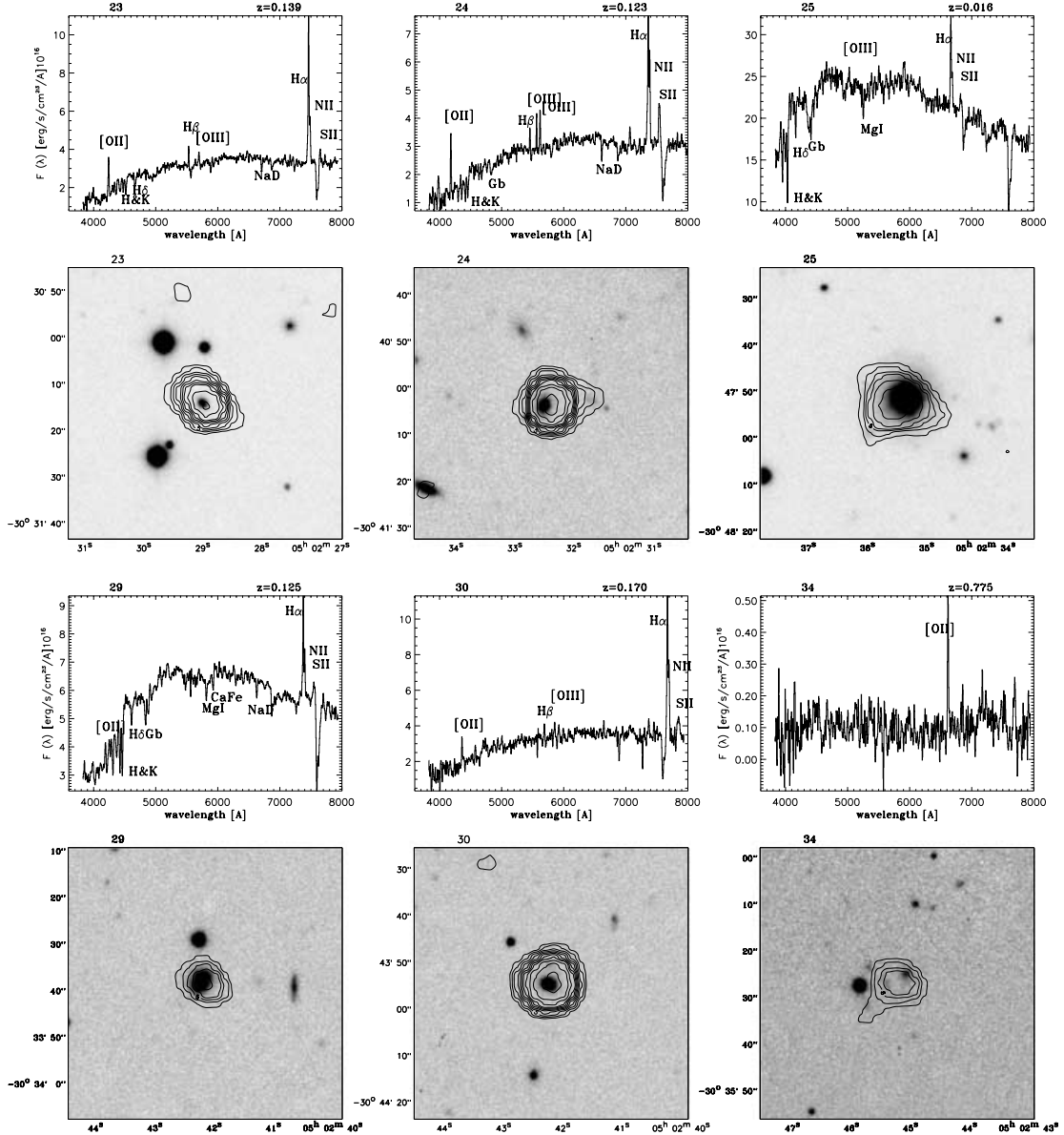


Figure 2 – continued

sample (only two objects have been found with no emission lines). In the deeper fields (Lockman Hole, HDF-N: Fadda et al. 2002; Alexander et al. 2002; Elbaz et al. 2002) constraints on the AGN contribution to the mid-infrared (MIR) sources have been provided from correlation analysis of deep X-ray and MIR observations. Although the total fraction of AGNs (type 1 and 2) does not appear to change with decreasing infrared flux, the fraction of AGN1 with respect to AGN2 (for which the IR emission is probably dominated by star formation activity in the host galaxy) seems to decrease significantly at faint fluxes (although the numbers of objects in all surveys is small). In fact, in S1 we find that ~ 15 per cent of identifications down to 1 mJy are AGN1, whereas in S2 (to ~ 0.7 mJy) this fraction is ~ 9 per cent (2/22) and becomes still smaller in the deeper Lockman field, ~ 5 per cent to 0.25 mJy.

In Fig. 5 we show the spectrum and the I and K' images of source no 17. Contour levels of the 15- μ m and of the radio emission are plotted superimposed to the two images, respectively. The source,

identified with a barred spiral at $z = 0.02$, is shown separately because of the large extension of its emission in the optical, radio and infrared bands ($\sim 0.5 \times 1$ arcmin 2). The infrared and radio emission are more pronounced in proximity of the spiral arms with respect to the galaxy centre. This is expected since IR and radio emission in spiral galaxies are tracers of star formation, which takes place preferentially in the spiral arms. For this reason the spectrum, which is dominated by the galactic bulge, does not show any emission lines. To retain consistent classification, this galaxy has been classified as an early-type galaxy in Table 3, despite its clear spiral morphology.

5 DISCUSSION

In this section we will describe the properties of our sample and, by making comparisons with other IR surveys, we will highlight the

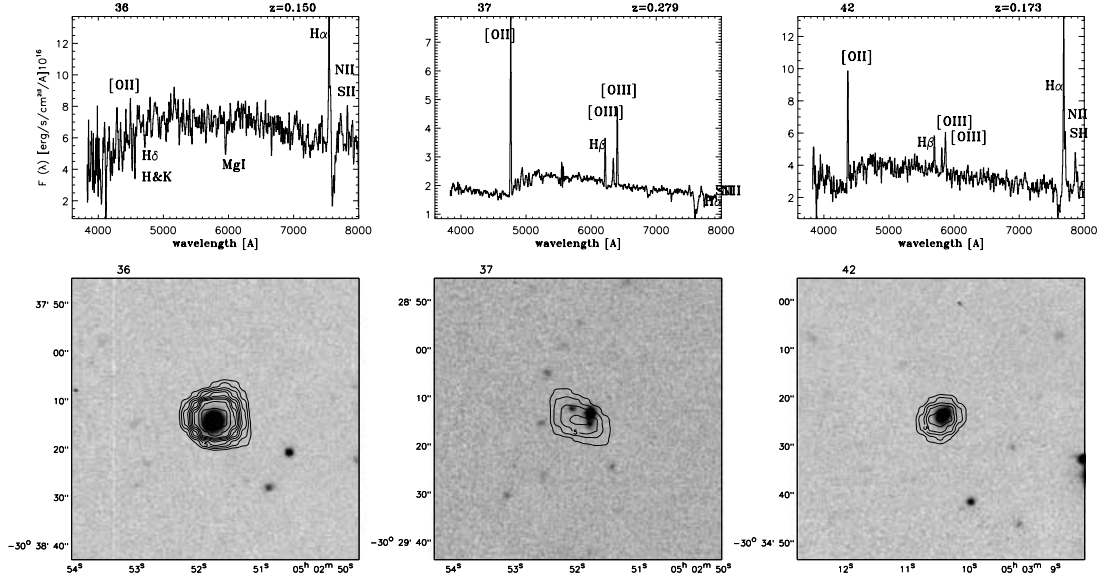


Figure 2 – continued

contribution of this work to the understanding of the nature of the IR sources.

First, the z and 15- μ m luminosity distributions of the S2 sources will be compared with those of deeper 15- μ m fields, to look for evolutionary effects. Secondly, the extinction affecting the sources will be estimated and the results compared with those obtained from a sample of local high-luminosity *IRAS* galaxies, to study possible variation of the amount of dust with IR luminosity. In this context, we will discuss the possible dependence of reddening on IR luminosity by studying the relation between $H\alpha$ and IR luminosities and comparing our results with those found in a recent work by Kewley et al. (2002). Finally, we will compute and compare the star formation rate (SFR) of our galaxies derived from the IR, $H\alpha$ and radio indicators.

5.1 Multiband and spectral properties

In Fig. 6 we present the I magnitude versus 15- μ m flux and the 15- μ m luminosity versus redshift diagrams. The objects are plotted with different symbols according to their spectral classification, as described in the caption. Objects not observed spectroscopically are represented by filled triangles, while objects with no optical counterpart to $I \sim 22$ are represented by vertical arrows. Our data are compared here with those from deeper surveys: HDF-S (crosses: Oliver et al. 2002; Mann et al. 2002) and HDF-N (diagonal crosses: Aussel et al. 1999). In both fields the percentage of spectroscopic identifications available in the literature is ~ 50 per cent. All the galaxies of the HDF-S field have been identified in I or near-IR bands (the objects not observed spectroscopically are represented by crosses inside circles). For all the data, the 15- μ m rest-frame luminosity have been derived by assuming the spectral energy distribution (SED) of M82 for galaxies and AGN2 and a typical Seyfert 1 SED for AGN1 (Franceschini et al. 2001).

In the 15- μ m– I diagram (Fig. 6, left-hand panel), the regions occupied, respectively, by stars and by extragalactic objects are well separated by the dashed line which represents the MIR-to-optical ratio $R = 2.5$, where R is defined as $R = S \times 10^{(m-12.5)/2.5}$ (S is the 15- μ m flux in mJy, while m is the optical magnitude in the I band). As also found by Gruppioni et al. (2002), the fraction of

stars still stays at ~ 20 –30 per cent for 15- μ m flux densities fainter than ~ 1 mJy.

The starburst population is the dominant population at faint 15- μ m flux densities and weak optical magnitudes. The four S2 sources without I counterparts to $I \sim 22$ and the two HDF-S sources at fainter magnitudes ($I \sim 22$), might belong to a separate population of objects characterized by faint optical magnitudes and/or high redshifts. A similar indication is also found in the redshift–magnitude distribution of sources in the S1 survey (La Franca et al. 2003, in preparation), where a second optically fainter population appears at $R \gtrsim 21.5$, well separated from the bulk of the extragalactic sample.

In Fig. 7 we report the redshift distribution of the sources in the different surveys to highlight the redshift ranges that these different samples cover.

As shown in Fig. 6 (right-hand panel) and Fig. 7, most of the spectroscopically identified extragalactic sources in S2 are at low-to-moderate redshifts ($z \lesssim 0.3$), though two starburst galaxies and two AGN2 are up to $z \sim 0.7$. The higher-redshift objects are, as expected, the two AGN1. In our analysis we consider AGN2 together with star-forming galaxies, according to the idea that for both populations the IR spectrum may be dominated by starburst emission (Franceschini et al. 2001). The median redshift of the S2 sources (excluding the two AGN1) is 0.17 ± 0.06 ($\sigma_{\text{med}} = 1.2533\sigma/\sqrt{N}$, Akin & Colton 1970), while in the HDF-S and HDF-N the median redshifts are significantly higher (~ 0.5 and ~ 0.6 , respectively).

Considering the sample of sources with flux density ≥ 0.8 mJy (which is spectroscopically complete, see the left-hand panel in Fig. 6), we have compared the observed redshift distribution, corrected for incompleteness by weighting each source for the corresponding effective area, with the distribution predicted by the model fitting the source counts (see Gruppioni et al. 2002). The model of Gruppioni et al. (2002) has been obtained by re-adapting the model of Franceschini et al. (2001), for which the IR sources can be divided into three different populations with different evolutionary properties: non-evolving normal spiral, strongly evolving starburst plus AGN2 and evolving AGN1. While the observed and the predicted z distributions for the star-forming sources are in good agreement at $z \lesssim 0.5$ (first peak of the predicted redshift distribution, see

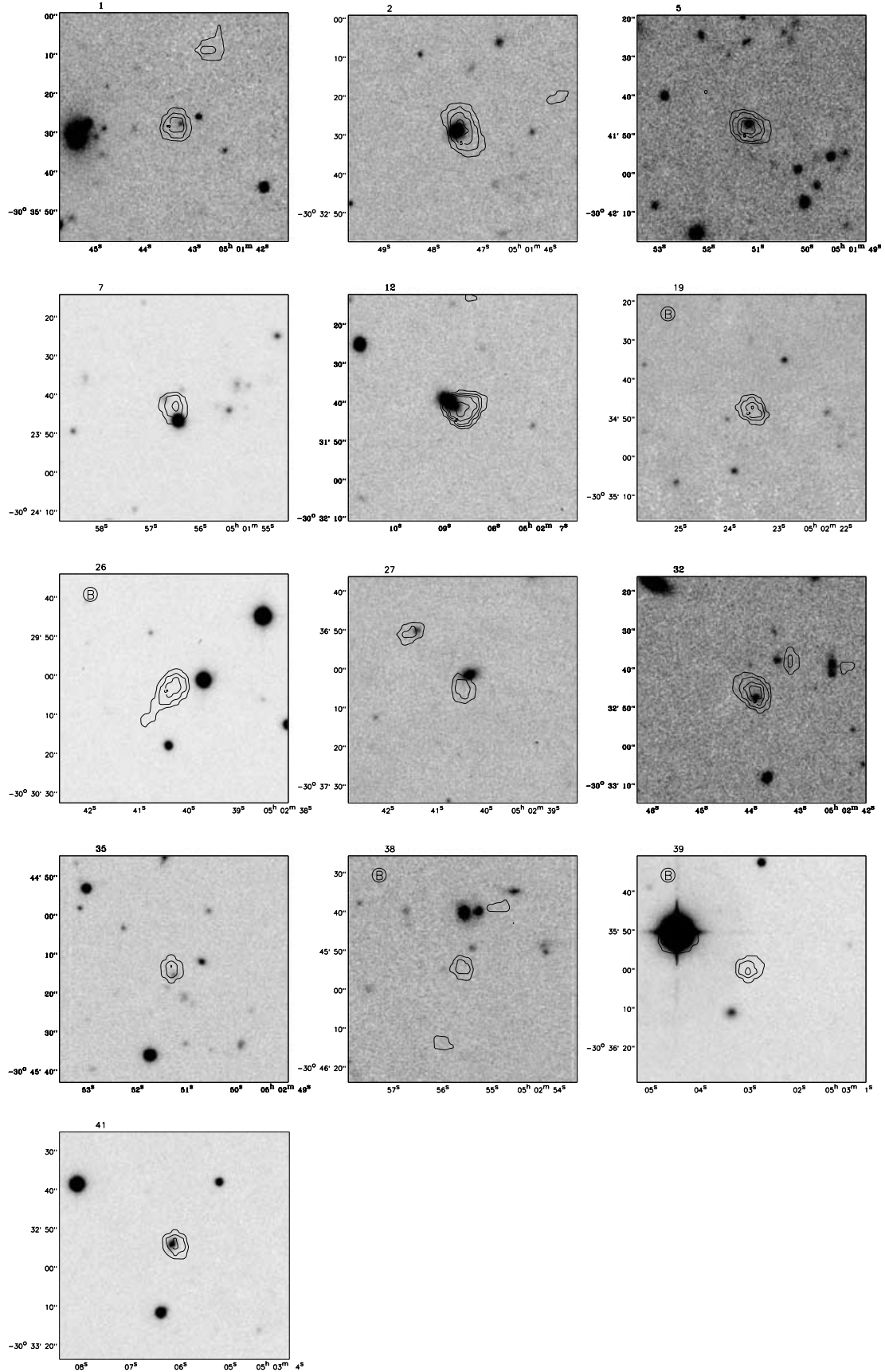


Figure 3. *I*-band CCD images of the 13 sources with no spectral information and not classified as stars. A ‘B’ symbol in the top left-hand corner of the thumbnails indicates an optically blank object (sources nos 19, 26, 38 and 39). The size of each image is $1 \times 1 \text{ arcmin}^2$. Contour levels of the 15- μm emission corresponding to $[3, 4, 5, 6, 7, 8, 9, 10, 12, 15, 20, 25, 30, 50, 100]\sigma$ are superimposed on each optical image.

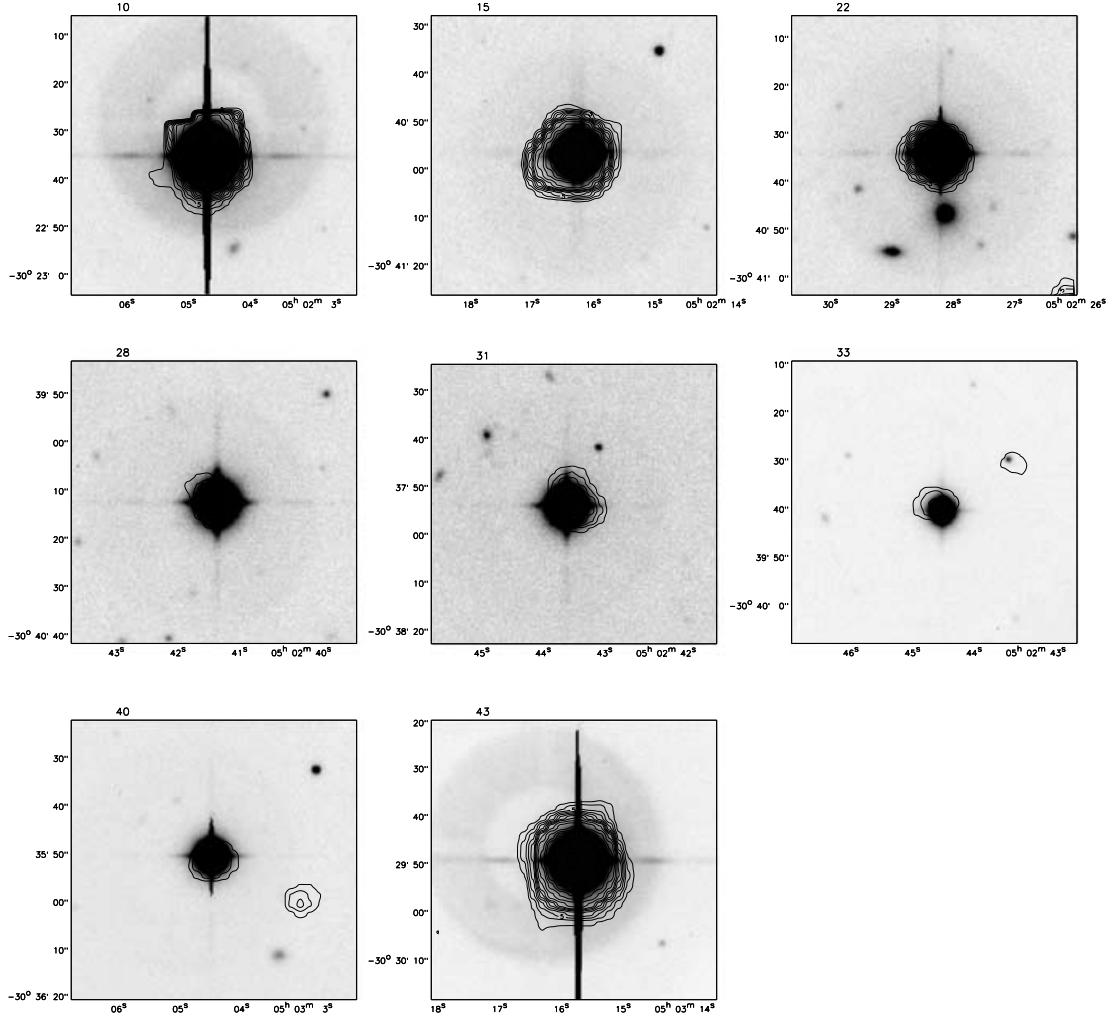


Figure 4. *I*-band CCD images of the eight sources with no spectral information and classified as stars from the photometric data. Sources 10, 15, 22, 28, 40 and 43 have also been found in the stellar Tycho-2 catalogue (Hog et al. 2000). The size of each image is 1×1 arcmin². Contour levels of the 15- μ m emission corresponding to $[3, 4, 5, 6, 7, 8, 9, 10, 12, 15, 20, 25, 30, 50, 100]\sigma$ are superimposed on each optical image.

fig. 12 in Gruppioni et al. 2002), the number of star-forming galaxies predicted by the model at $z > 0.5$ is higher (~ 50 per cent) than observed (~ 20 per cent). The discrepancy would be even larger without considering the luminosity break in the LLF of local starburst galaxies proposed by Gruppioni et al. (2002). Disagreement between the predicted and the observed z distributions is found also in the HDF-S field, where the observed z distribution (Mann et al. 2002) is shifted to lower redshift than expected by the model and observed in the HDF-N (see Franceschini et al. 2001). A possible cause for this disagreement between the observed and the predicted distributions in both S2 and HDF-S could be the low statistics at high z in S2 (only two sources with $S \geq 0.8$ mJy have $z \gtrsim 0.5$) or the spectroscopic incompleteness and the cosmic variance affecting small fields in the HDF-S (area ~ 20 arcmin²). Only complete z distributions in larger 15- μ m fields (such as ELAIS main fields or Lockman shallow) not affected by small-area variations will provide more stringent constraints for testing the model predictions. Only with such data, it will be possible to eventually modify the model according to the observational constraints.

The majority of our galaxies + AGN2 objects (18/20, ~ 90 per cent) have an IR luminosity [$L_{\text{IR}} = L(8\text{--}1000\text{ }\mu\text{m})$] typical of ‘starburst’ galaxies ($10^{10} < L_{\text{IR}} \leq 10^{11} L_{\odot}$) or luminous infrared galax-

ies (LIGs: $10^{11} < L_{\text{IR}} \leq 10^{12} L_{\odot}$), with no object with a luminosity clearly in the range of those typical of ultraluminous infrared galaxies (ULIGs: $L_{\text{IR}} > 10^{12} L_{\odot}$). The IR luminosities have been calculated from the 15- μ m ones using the relation $L_{\text{IR}} = 11.1 \times L_{15\text{ }\mu\text{m}}^{0.998}$ (Elbaz et al. 2002). The median luminosity of our galaxy + AGN2 sample is $L_{\text{IR}} = 10^{10.8 \pm 0.2} L_{\odot}$. As shown in Fig. 6 (right) a similar range in luminosities is also sampled by the deeper surveys (HDF-N and HDF-S), although for these surveys the bulk of the distribution is shifted towards higher luminosities ($\sim 10^{11.5} L_{\odot}$ in HDF-N). Given the spectroscopic incompleteness of all the samples considered, the unidentified objects could be either objects at similar redshift but absorbed or ULIGs at higher redshift. This suggests a possible trend of luminosity with z , with the galaxies at higher redshift being characterized by higher 15- μ m luminosity. Such a trend would be consistent with the sharp steepening observed in the 15- μ m source counts around 1–2 mJy (Elbaz et al. 1999; Gruppioni et al. 2002), which can be explained only under the hypothesis of strong evolution (both in density and luminosity) for IR galaxies.

In Fig. 8, the $U - B$ and $I - K$ colours versus redshift plots are shown. Panels (a) and (c) have no extinction correction, while panels (b) and (d) have been obtained assuming an average extinction

Table 3. Spectroscopic results and $H\alpha$, 15- μ m and 1.4-GHz rest-frame luminosities of the 15- μ m sources in the S2 field.

<i>N</i>	<i>z</i>	EW ([O II]) (Å)	EW (H δ) (Å)	EW (H α) (Å)	S (H α) (erg cm ⁻² s ⁻¹) 10 ¹⁶	L (H α) (L _⊙)	L (15 μ m) (L _⊙)	L (1.4 GHz) (L _⊙)	Class
1									
2									
3	0.127	42	<4	73*	34.7	8.12	9.81	4.69	Starburst
4	0.050		<4				9.05	3.90	Early type
5									
6	1.813						13.06		AGN1
7									
8	0.600	65	<4	out			10.78		Starburst
9	0.308	7	4-5	out			10.19	5.37	Spiral
10	0								Star
11	0.628	49	<4	out			10.98		AGN2
12									
13	0.450	6	<4	out			10.68	5.23	AGN2
14	0.862						12.19	5.91	AGN1
15	0								Star
16	0.127	36	<4	47	5.0	6.90	9.33	4.27	Spiral
17	0.020	out	<4				8.36	2.71	Early type
18	0.111	43	<4	37	18.3	7.50	9.44	4.51	Starburst
19									
20	0.191	32	<4	63	8.7	7.96	10.28	5.43	Spiral
21	0.191	12	5	32*	20.0	7.99	10.14	5.15	Spiral
22	0								Star
23	0.139	22	4-5	51*	17.9	7.44	9.48	4.23	Spiral
24	0.123	25	<4	36	4.2	6.91	9.52	4.16	Spiral
25	0.016	out	<4	15	28.8	5.97	7.74	2.41	Spiral
26									
27									
28	0								Star
29	0.125	4	<4	11*	6.7	7.31	9.15		Spiral
30	0.170	19	<4	57	13.0	7.73	9.89	5.01	Spiral
31	0								Star
32									
33	0								Star
34	0.775	47	<4	out			10.95	6.60	Starburst
35									
36	0.150	11	5	45*	20.2	7.99	9.66	4.76	Spiral
37	0.279	45	<4	out			9.83	4.97	Starburst
38									
39									
40	0								Star
41									
42	0.173	45	<4	79*	21.8	7.93	9.41	4.60	Starburst
43	0								Star

Notes. Column 1: the ISO source number. Column 2: the measured spectroscopic redshift. Columns 3–5: the equivalent widths at rest of [O II] ($\lambda = 3727$ Å) and $H\alpha$ ($\lambda = 6563$ Å) in emission, $H\delta$ ($\lambda = 4101$ Å) in absorption. The (*) symbol in column 5 indicates galaxies for which EW($H\alpha$) and $S(H\alpha)$ have been measured directly. Column 6: $H\alpha$ fluxes. Columns 7–9: $H\alpha$, 15- μ m and 1.4-GHz luminosities. $H\alpha$ luminosities have been corrected for aperture losses but not for extinction effects (see Section 5 for more details). Column 10: the spectral classification.

from stellar continuum of $E_s(B - V) \sim 0.2$. As shown in the plots, galaxies with star formation cover a wide range of colours but, if not corrected for extinction, they are on average redder than expected (a large fraction of objects are above the evolutionary curve of early-type galaxies). Using the extinction curves of Calzetti et al. (2000), we have derived the extinction expected in different bands for different values of the colour excess $E_s(B - V)$. This was done for each galaxy separately, depending on its own redshift. An extinction of $E_s(B - V) \sim 0.2$ – 0.3 seems to be necessary to bring back the objects to the intrinsic colours expected for late-type/starburst objects. Following Calzetti et al. (2000), an extinction of $E_s(B - V) \sim 0.2$ – 0.3 derived from the stellar continuum corresponds to

an extinction derived from the Balmer decrement $H\alpha/H\beta$ of $E(B - V) \sim 0.4$ – 0.6 . Such an amount of extinction is lower than that found by PW00 analysing a sample of local very luminous infrared galaxies (VLIRG: $L_{\text{IR}} > 10^{11.15} L_{\odot}$, $H_0 = 75 \text{ km s}^{-1} \text{ Mpc}^{-1}$), who derive $E(B - V) \sim 0.8$ – 1.0 from the Balmer decrement $H\alpha/H\beta$. The indication that the extinction affecting the lines is an increasing function of the IR luminosity is also highlighted in Fig. 9, where the EW([O II])/EW($H\alpha$ + [N II]) ratio is plotted as a function of L_{FIR} for both our data and PW00 data (see the next section for the derivation of L_{FIR} from $L_{15\mu\text{m}}$). The median values of the ratio are 0.33 and 0.21, respectively, for S2 and the VLIRG sample (the two distributions differ at a 2σ level from a KS test). In the scenario proposed

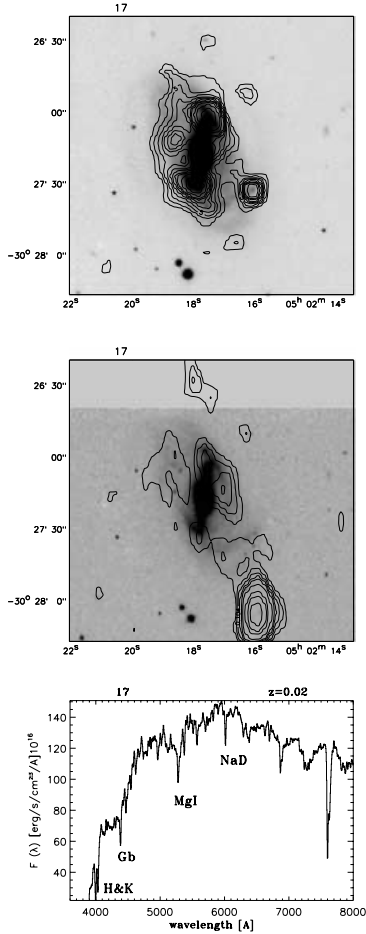


Figure 5. Top panel: optical *I*-band image of source no 17 with superimposed the contour levels of the 15- μ m emission corresponding to [3, 4, 5, 6, 7, 8, 9, 10, 12, 15, 20, 25, 30, 50, 100] σ . The size of the image is 2×2 arcmin². Central panel: as in the top panel with the contour levels of the radio emission ([2, 3, 4, 5, 6, 8, 12, 15, 20, 30, 50, 75, 100] σ) superimposed on the *K'* image. Bottom panel: EFOSS2 spectrum of the source.

by Poggianti et al. (1999) low values of the EW ratios are due to high dust extinction, since the [O II] emission line is more affected by dust than the H α one. The continuum underlying the lines is produced by older, less extinguished stars and, consequently, the net result is a low EW ratio of the two lines. The anticorrelation between the EW([O II])/EW(H α + [N II]) ratio and the IR luminosity (see also Kewley et al. 2002) is consistent with the result found recently in the *B* band, where a similar trend between this ratio and the luminosity in the *B* band has been found (Jansen, Franx & Fabricant 2001; Charlot et al. 2002).

5.2 Star formation rates

In this section we compute and compare the star formation rate derived from three different indicators: the far-infrared (FIR) luminosity, the radio luminosity and the H α luminosity. The FIR luminosity has been derived by assuming a value of 5 for the $L_{\text{FIR}}/L_{15\mu\text{m}}$ ratio. Such a ratio is an average value estimated in the ELAIS field S1, representing typical starburst galaxies slightly more active than M82 (see also Elbaz et al. 2002). The radio luminosity has been derived assuming a power-law spectrum with a spectral index $\alpha \sim 0.7$ ($S_\nu \propto \nu^{-\alpha}$). Finally, the H α luminos-

ity has been derived from the observed fluxes of the H α line (see Table 3).

To correct for the flux losses caused by observing only the nuclear region of the galaxies (the slit width is 1.2–1.5 arcsec, see Section 4.1), we have assumed that the H α line emission and the optical light are correlated over the entire galaxy; we have then corrected the spectra fluxes for the ratio between the $R_{63\text{F}}$ magnitudes from APM and the equivalent magnitudes derived from spectra (hereafter called R'). We have estimated the R' magnitudes by integrating the spectra over a standard Cousins R_c filter and then we have reported the R_c magnitude to APM magnitudes ($R_{63\text{F}}$) following Bessel (1986) ($R_c - R_{63\text{F}} \sim 0.1$ for $R - I \sim 0.7$ as found for our galaxies, see Table 2). In Fig. 10 (top) the result of the comparison is reported. The flux losses range from ~ 0.5 mag for the weaker sources ($R_{63\text{F}} \sim 19$ –20) to ~ 1.5 mag for the brighter ones ($R_{63\text{F}} \sim 17$ –18). This trend corresponds to a trend in the typical angular sizes of the sources, from 1 to 2 arcsec (i.e. sources 8 and 13, Fig. 2) to several arcsecs (i.e. sources 21 and 36, Fig. 2). Considering the sources with no APM counterpart, a correction of 0.5 mag has been applied to sources below the APM limit, while a correction of 1 mag has been applied to extended sources with unreliable APM magnitudes (see Table 2).

Fig. 10 (bottom) shows the H α luminosity corrected for aperture effects versus the FIR luminosity. The filled circles represent our data with no distinction between the different galaxy classes (type 1 AGN have been excluded). The empty diamonds are the data of Kewley et al. (2002) for a sample of galaxies in the Nearby Field Galaxy Survey (NFGS) with *IRAS* detections. The empty triangles are the data from PW00 after applying the maximum correction suggested by the authors (a factor of 7, see PW00). The plot shows a strong correlation between the two luminosities over more than four orders of magnitude; the large dispersion of the PW00 data is probably caused by the application of a unique average aperture correction. The solid and dot-dashed lines show the best-fitting relations between the two luminosities found, respectively, in this work and by Kewley et al. (2002) (in both cases using the FITXY routine from Numerical Recipes – Press et al. 2002). This routine uses the linear least-squares minimization and includes error estimates for both variables. We derived the FIR luminosity uncertainties by propagating the measured errors on 15- μ m fluxes (see Table 1), while we assumed errors of ~ 30 per cent for the H α luminosities (as estimated from the EW measures). The resulting relation for our data has the form $\log[L(\text{H}\alpha)] = (0.88 \pm 0.07) \log[L(\text{FIR})] - (1.5 \pm 0.7)$. Though only indicative, our result shows a slope lower than 1 (2σ level), in agreement with the result of Kewley et al. (2002), who find a slope equal to 0.77 ± 0.04 . This suggests that the ratio between IR and H α luminosities is a function of the luminosity itself. Kewley et al. (2002) have shown how this effect could be attributed to the reddening $E(B - V)$, finding that the IR to H α luminosity ratio is a strong function of reddening $E(B - V)$ (see also Hopkins et al. 2001).

To convert the H α luminosities to star formation rates, we use the calibrations given by Kennicutt (1998) for a Salpeter (1955) initial mass function (IMF) running from 0.1 to $100 M_\odot$. To convert the IR and 1.4-GHz luminosities to star formation rates, we use the calibration given by Cram et al. (1998) (see also Condon 1992), scaled to the same IMF and mass range of Kennicutt (1998) following Mann et al. (2002).³

³ Condon's (1992) relations are based on a Miller & Scalo (1979) IMF over [5, 100] M_\odot .

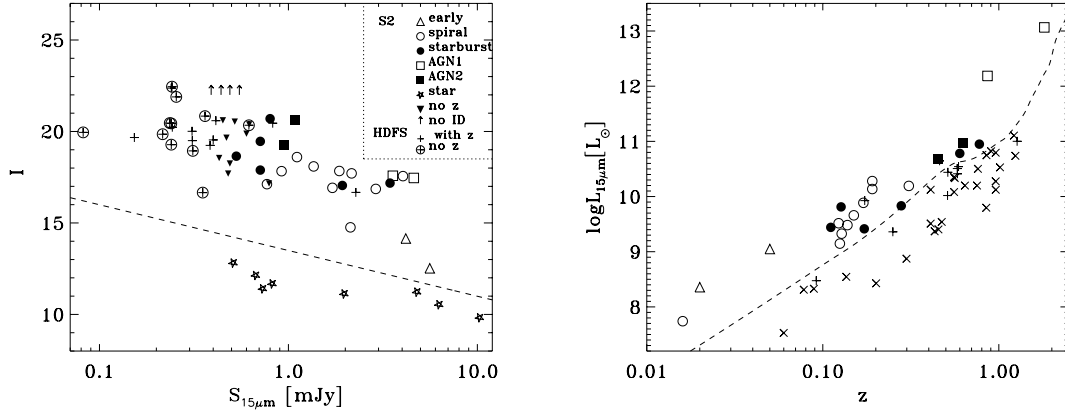


Figure 6. Left-hand panel: I magnitudes versus 15- μm flux densities for the S2 and HDF-S sources. The different symbols represent the different spectroscopic classes of objects: empty triangles denote early galaxies, empty circles for normal spiral galaxies, filled circles for starburst galaxies, squares for AGNs (empty for type 1 and filled for type 2) and star symbols for stars. The filled triangles denote the objects not observed spectroscopically, while the vertical arrows are for sources with no optical counterparts. A line of constant ratio between 15- μm and I -band flux, which separates stars from extragalactic objects is also reported. As a comparison, the data from the HDF-S are included: the crosses represent the objects spectroscopically identified, while the crosses inside circles represent the objects not observed spectroscopically (Mann et al. 2002). Right-hand panel: 15- μm rest-frame luminosity (in solar units) versus redshift. Symbols are the same as for the left-hand panel. In this figure the data from the HDF-N are also included (diagonal crosses, Aussel et al. 1999). The dashed line corresponds to the minimum detectable luminosities at different z in S2, considering a limiting flux of 0.5 mJy and the 15- μm K -correction of M82.

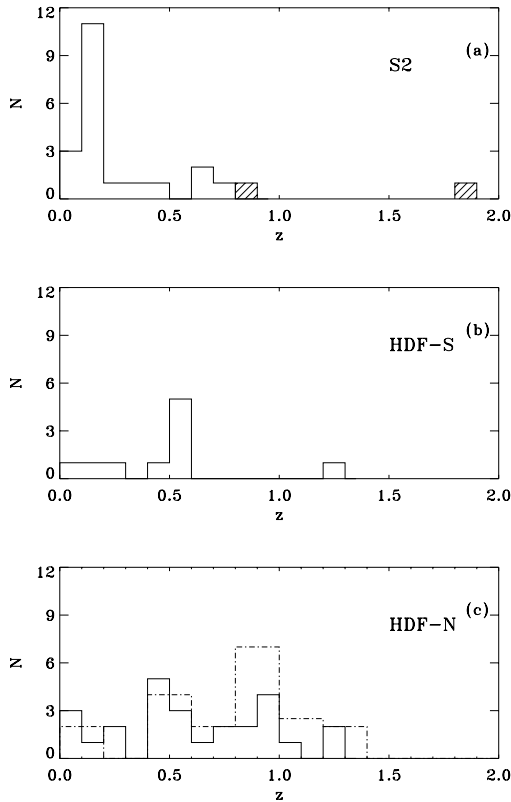


Figure 7. Redshift distributions of the 15- μm sources in S2 (a, the hatched area represent the AGN1 objects), in the HDF-S (b, Mann et al. 2002) and in the HDF-N surveys (c, continuous line from Aussel et al. 1999; dashed line from Franceschini et al. 2001).

The set of estimators considered are:

$$\text{SFR}_{\text{H}\alpha} = 7.9 \times 10^{-35} L(\text{H}\alpha) (\text{W})$$

$$\text{SFR}_{\text{FIR}} = 0.9 \times 10^{-23} L_\nu(60 \mu\text{m}) (\text{W Hz}^{-1})$$

$$\text{SFR}_{1.4\text{GHz}} = 1.1 \times 10^{-21} [\nu(\text{GHz})]^\alpha L_\nu(1.4\text{GHz}) (\text{W Hz}^{-1})$$

The FIR luminosity has been converted to 60- μm luminosity ($L_{\text{FIR}} \sim 1.3 \times L_{60\mu\text{m}}$), by considering the definition of the FIR flux given by Helou et al. (1988) [$\text{FIR} = 1.26(2.58S_{60\mu\text{m}} + S_{100\mu\text{m}})10^{-14}$ (W m^{-2})], the FIR–1.4-GHz relation (‘q’ parameter; Condon 1992; Yun, Reddy & Condon 2001) and the 1.4-GHz–60 μm relation ($S_{60\mu\text{m}} \sim 127S_{1.4\text{GHz}}$, Cram et al. 1998).

In Fig. 11, the star formation rate derived from 1.4 GHz (left) and from $\text{H}\alpha$ (right) are compared with the SFR obtained from FIR emission. The $\text{H}\alpha$ estimates are not corrected for extinction. As found by Condon (1992), the star formation rates deduced from the FIR and the decimetric radio luminosities are well correlated. Moreover, approximately the same relation found locally by Condon (1992) is still valid at the redshifts sampled by our data ($z_{\text{med}} \sim 0.2$). For a detailed study of the radio/mid-IR correlation see the study of Gruppioni et al. (2003) for the ELAIS sources and the works of Garrett (2002) and Bauer et al. (2002) for the HDF-N and the CDF-N sources.

The same level of agreement is not found between the $\text{H}\alpha$ and the FIR indicators, since the SFR based on $\text{H}\alpha$ are a factor of ~ 5 –10 lower than the SFR based on FIR (see also Cram et al. 1998 for a detailed discussion). The two indicators agree after applying the mean extinction correction suggested by the Balmer decrements and the optical colours [$E(B - V) \sim 0.5$, $A(\text{H}\alpha) \sim 2.0$] to the $\text{H}\alpha$ estimates. A correction of ~ 2 mag is intermediate between the correction of 1 mag found by Kennicutt (1983) for a sample of local spirals and the correction of ~ 2.5 –3 mag found by PW00 for the sample of local very luminous infrared galaxies, indicating, as mentioned previously, that the extinction suffered by galaxies is an increasing function of IR luminosity.

Further evidence supporting this hypothesis is supplied by the comparison of the SFR rates computed in this work with those of Rigopoulou et al. (2000), who have studied the infrared and $\text{H}\alpha$ properties of a subsample of HDF-S ISOCAM galaxies at high redshift and high IR luminosities ($\langle z \rangle \sim 0.62$, $\langle L_{\text{FIR}} \rangle \sim 10^{11.4}$, $H_0 = 75 \text{ km s}^{-1} \text{ Mpc}^{-1}$). They find that SFR estimates from not-corrected $\text{H}\alpha$ are lower than the FIR ones by a factor of 5–50 and that a reddening correction of ~ 3 mag is necessary to bring the $\text{H}\alpha$ and FIR rates to the same scale.

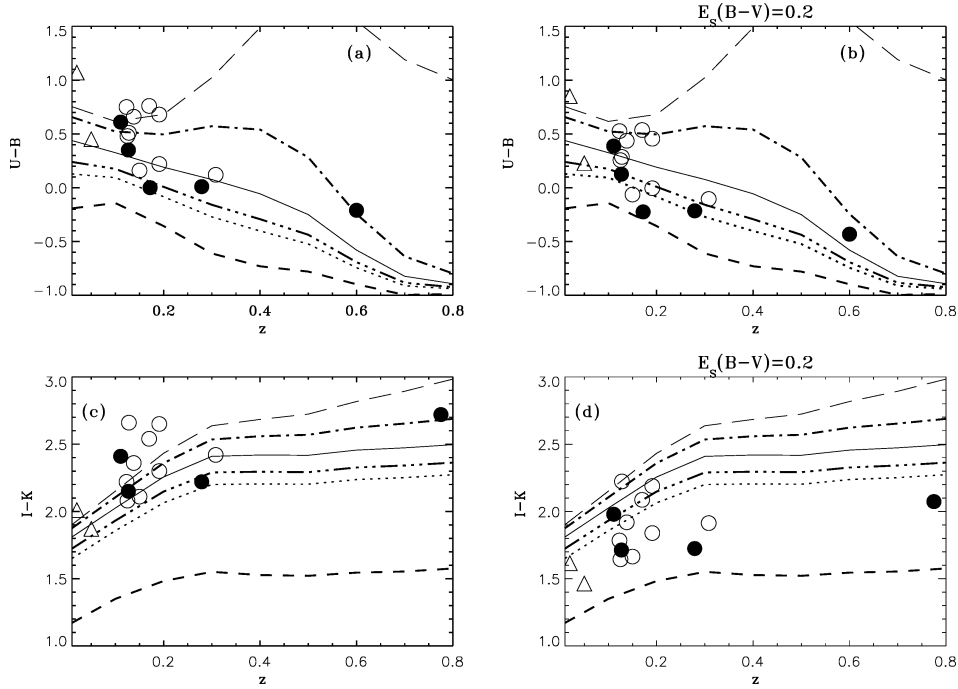


Figure 8. $U - B$ (a, b) and $I - K$ (c, d) colours versus redshift diagrams for our galaxies. The different curves correspond to the colour–redshift relations for evolved galaxies derived from the Bruzual & Charlot (1993) models and represent models for early-type galaxies (long-dashed line), S0 galaxies (dot-dashed line), Sab–Sbc spirals (solid and dot-dot-dot-dashed line), Scd (dotted line) and irregular (dashed line) galaxies. The curves, kindly provided by L. Pozzetti, have been computed using the appropriate filter (U , B , I and K) transmission used in our observations. The parameters of the models are given in Pozzetti, Bruzual & Zamorani (1996). In (a) and (c) no extinction correction has been applied. In (b) and (d) colours have been corrected using the reddening curve of Calzetti et al. (2000) with an extinction of $E_s(B - V) = 0.2$.

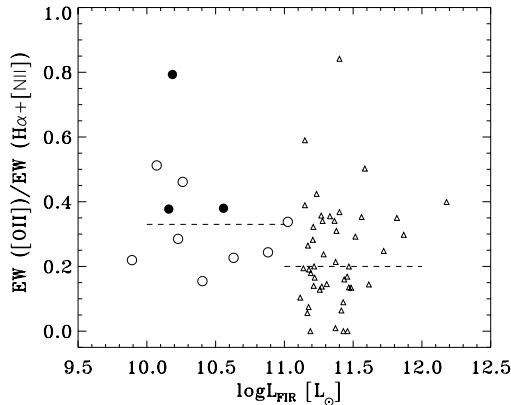


Figure 9. $\text{EW}([\text{O II}])/\text{EW}(\text{H}\alpha + [\text{N II}])$ ratio as a function of L_{FIR} for our data (circles) and for the sample of PW00 (empty triangles). The dashed lines correspond to the median values of the ratio (0.33 and 0.21, respectively) for the two samples.

6 CONCLUSIONS

We have studied the properties of a new sample of 15- μm sources detected in the ELAIS Southern field, S2, using the *Lari method* of reduction (see L01). The 15- μm catalogue constitutes 43 sources with fluxes between 0.4 and 10 mJy and hence is perfectly suited to investigate the properties of sources in the flux density region where the 15- μm source counts are observed to diverge from Euclidean predictions (2–3 mJy: Elbaz et al. 1999; Gruppioni et al. 2002).

A high percentage of sources (~ 90 per cent) have a reliable optical identification brighter than $I \sim 21$ mag and for 21 objects a

radio counterpart has been found. Eight bright sources have been classified as stars from the photometric data, while spectra have been obtained for 22 extragalactic objects, reaching a high identification percentage (30/43, ~ 70 per cent). All but one of the 28 sources with 15- μm flux density > 0.7 mJy are identified. Given the good spectral quality, we were able to determine object type, redshift, equivalent width of the main lines and $\text{H}\alpha$ fluxes. The majority of the sources are star-forming galaxies (18 out of 22 objects, ~ 82 per cent) with 15- μm luminosities typical of ‘starburst’ and luminous infrared galaxies. AGN (type 1 and 2) constitute ~ 18 per cent of the extragalactic sample, while the fraction of early-type galaxies is small (~ 9 per cent). The median luminosity of our galaxies + AGN2 objects is $L_{\text{IR}} = 10^{10.8 \pm 0.2} L_{\odot}$, while their median redshift is 0.17 ± 0.06 .

In comparison with deeper published 15- μm surveys (HDF-S: Mann et al. 2002; Oliver et al. 2002; HDF-N: Aussel et al. 1999), the S2 galaxies are at a lower redshift ($z_{\text{med}} \sim 0.2$ instead of 0.5 and 0.6) and lower luminosities (the HDF-N has a peak around $\sim 10^{11.5} L_{\odot}$). However, a more detailed comparison of the properties of the sources in the three samples would require a higher level of completeness in the spectroscopic identification (S2 is ~ 70 per cent complete, while HDF-S, HDF-N are ~ 50 per cent complete).

We have compared the 15- μm and $\text{H}\alpha$ luminosities corrected for aperture losses but not for extinction. Consistent with the results from Kewley et al. (2002), we have found an indication that the ratio between 15- μm and $\text{H}\alpha$ luminosities not corrected for extinction increases with luminosity, suggesting that the amount of reddening is not constant, but is a function of luminosity, the more luminous galaxies being the more affected by extinction.

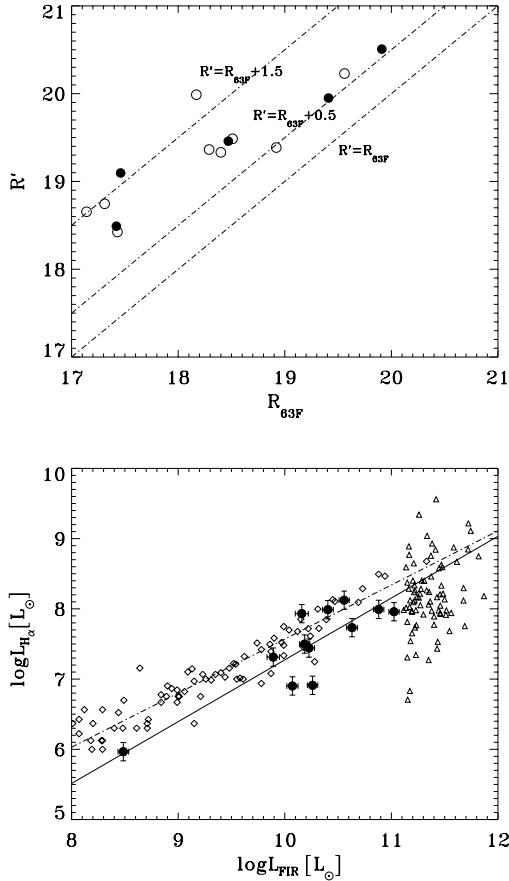


Figure 10. Top: relation between nuclear R magnitude (R') and total R magnitude (R_{63F}). The three dot-dashed lines indicate differences of 0.0 (lower), 0.5 (central) and 1.5 mag (upper). Bottom: $H\alpha$ versus FIR rest-frame luminosity (in solar units). The filled circles represent our data with no distinction between the different classes (AGN1 have been excluded). The empty diamonds are from Kewley et al. (2002) for a sample of galaxies detected by *IRAS* in the NFGS. The empty triangles are from PW00, after applying the larger possible aperture correction (a factor of 7). The solid and dot-dashed lines show, respectively, the fits between the two luminosities from this work and from Kewley et al. (2002).

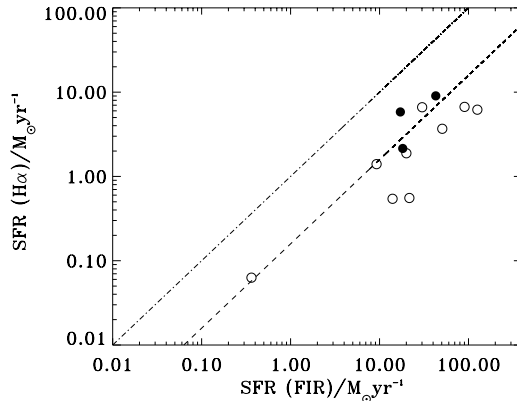
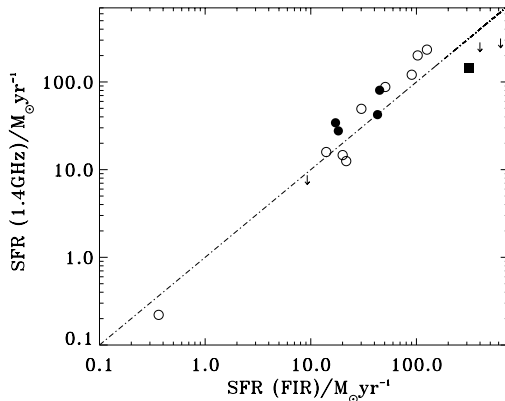


Figure 11. Left: SFR from 1.4 GHz versus SFR from FIR. Symbols are the same as in Fig. 6. The vertical arrows are the radio 3σ upper limits. The relation corresponding to $\text{SFR}(1.4 \text{ GHz}) = \text{SFR}(\text{FIR})$ is shown as a dot-dashed line. Right: SFR from no-extinction-corrected $H\alpha$ versus SFR from FIR. The dot-dashed line shows the relation $\text{SFR}(H\alpha) = \text{SFR}(\text{FIR})$ and the dashed-line is found for an average extinction of $E(B - V) = 0.5$ [$A(H\alpha) = 2$].

Using the 15- μm , radio and $H\alpha$ luminosities, we have derived the star formation rates and we have compared the results obtained with the three different indicators. We have found a tight linear relation between radio and 15- μm -based star formation estimates. This indicates that the well-studied local radio/FIR correlation (Condon 1992) is still valid at the median redshift of our sample ($z_{\text{med}} \sim 0.2$). The derived star formation values typically range between 10 and $200 \text{ M}_{\odot} \text{ yr}^{-1}$, with a median value of $\sim 40 \text{ M}_{\odot} \text{ yr}^{-1}$. Estimates based on the $H\alpha$ luminosities tend to be more scattered and to lie about a factor of 10 below the trend defined by the radio/FIR estimates. An average correction of ~ 2 mag is necessary to bring the $H\alpha$ estimates on the same scale as the other indicators. This correction is consistent with the average extinction correction derived from the Balmer decrements and from the optical colours (assuming the Calzetti et al. 2000 reddening curve) and is intermediate between the extinction found for local spiral galaxies (Kennicutt 1983) and the extinction found by PW00 for a sample of local very luminous infrared galaxies.

ACKNOWLEDGMENTS

This research was supported by the Italian Ministry for University and Research (MURST) under grants COFIN01 and by the Agenzia Spaziale Italiana (ASI) under contract no ASI-I/R/27/00. We thank Lucia Pozzetti for kindly providing colour-redshift models for different types of galaxy and helpful discussion, and Lisa Kewley for kindly providing data relative to the Nearby Field Galaxy Survey. We thank the referee David Alexander for his careful reading of the manuscript, interesting comments and suggestions, which greatly improved the quality of the paper.

REFERENCES

- Akin H., Colton R.R., 1970, *Statistical Methods*, 5th edn. Barnes & Nobles, New York
- Alexander D.M., Aussel H., Bauer F.E., Brandt W.N., Hornschemeier A.E., Vignali C., Garmire G.P., Schneider D.P., 2002, *ApJ*, 568, 85L
- Aussel H., Cesarsky C.J., Elbaz D., Starck J.L., 1999, *A&A*, 342, 313
- Bauer F.E. et al., 2002, *AJ*, 123, 1163
- Bessel M.-S., 1986, *PASP*, 98, 1303

- Bondi M. et al., 2003, *A&A*, 403, 857
 Calzetti D., Armus L., Bohlin R.-C., Kinney A.-L., Koornneef J., Storchi-Bergmann T., 2000, *ApJ*, 533, 682
 Ciliegi P., Zamorani G., Hasinger G., Lehmann I., Szokoly G., Wilson G., 2003, *A&A*, 398, 901
 Charlot S., Kauffmann G., Longhetti M., Tresse L., White S.D.M., Maddox S.J., Fall S.M., 2002, *MNRAS*, 330, 876
 Chary R., Elbaz D., 2001, *ApJ*, 556
 Condon J.-J., 1992, *ARA&A*, 30, 575
 Cram L., Hopkins A., Mobasher B., Rowan-Robinson M., 1998, *ApJ*, 507, 155
 Elbaz D. et al., 1999, *A&A*, 351, L37
 Elbaz D., Cesarsky C.J., Chanial P., Aussel H., Franceschini A., Fadda D., Chary R.R., 2002, *A&A*, 384, 488
 Fadda D., Flores H., Hasinger G., Franceschini A., Altieri B., Cesarsky C.J., Elbaz D., Ferrando Ph., 2002, *A&A*, 383, 838
 Flores H. et al., 1999, *ApJ*, 517, 148
 Franceschini A., Aussel H., Cesarsky C.-J., Elbaz D., Fadda D., 2001, *A&A*, 378, 1
 Garrett M.A., 2002, *A&A*, 384, 19
 Gruppioni C. et al., 1999, *MNRAS*, 305, 297
 Gruppioni C., Lari C., Pozzi F., Zamorani G., Franceschini A., Olver S., Rowan-Robinson M., Serjeant S., 2002, *MNRAS*, 335, 831
 Gruppioni C., Pozzi F., Zamorani G., Ciliegi P., Lari C., Calabrese E., La Franca F., Matute I., 2003, *MNRAS*, 341, L1
 Hamuy M., Walker A.R., Suntzeff N.B., Gigoux P., Heathcote S.R., Phillips M.M., 1992, *PASP*, 104, 533
 Hamuy M., Suntzeff N.B., Heathcote S.R., Walker A.R., Gigoux P., Phillips M.M., 1994, *PASP*, 106, 566
 Helou G., Khan I.-R., Malek L., Boehmer L., 1988, *ApJS*, 68, 151
 Hog E. et al., 2000, *A&A*, 357, 367
 Hopkins A.M., Connolly A.J., Haarsma D.B., Cram L.E., 2001, *AJ*, 122, 288
 Jansen R.A., Franx M., Fabricant D., 2001, *ApJ*, 551, 825
 Kennicutt R.-C., 1983, *ApJ*, 272, 54
 Kennicutt R.-C., 1992, *ApJ*, 388, 310
 Kennicutt R.-C., 1998, *ARA&A*, 36, 189
 Kewley L.J., Geller M.J., Jansen R.A., Dopita M.A., 2002, *AJ*, 124, 3135
 Kinney A.L., Calzetti D., Bohlin R.C., McQuade K., Storchi-Bergmann T., Schmitt H.R., 1996, *ApJ*, 467, 38
 Lari C. et al., 2001, *MNRAS*, 325, 1173 (L01)
 Lari C., Vaccari M., Fadda D., Rodighiero G., 2002, in Gry C. et al., eds, *Proc. Exploiting the ISO DATA Archive*, ESA Publications Series (SP-511), to be published
 Maddox S.J., Efstathiou G., Sutherland W.J., Loveday J., 1990, *MNRAS*, 243, 692
 Mann R.G. et al., 2002, *MNRAS*, 332, 549
 Matute I. et al., 2002, *MNRAS*, 332, L11
 Miller G.E., Scalo J.M., 1979, *ApJS*, 41, 513
 Oliver S. et al., 2000, *MNRAS*, 316, 749
 Oliver S. et al., 2002, *MNRAS*, 332, 5360
 Poggianti B.-M., Smail I., Dressler A., Couch W.-J., Barger A.-J., Butcher H., Ellis R.-S., Oemler A. Jr, 1999, *ApJ*, 518, 576
 Poggianti B.-M., Wu H., 2000, *ApJ*, 529, 157 (PW00)
 Pozzetti L., Bruzual G., Zamorani G., 1996, *MNRAS*, 281, 953
 Press W.H., Teukolsky S.A., Vetterling W.T., Flannery B.P., 2002, *Numerical Recipes in C: The Art of Scientific Computing*, 2nd edn. Cambridge Univ. Press, Cambridge
 Rigopoulou D. et al., 2000, *ApJ*, 537, L85
 Rowan-Robinson M., 2001, *ApJ*, 549, 745
 Salpeter E.E., 1955, *ApJ*, 121, 161
 Sutherland W., Saunders W., 1992, *MNRAS*, 259, 413
 Xu C., 2000, *ApJ*, 541, 134
 Yun M.S., Reddy N.A., Condon J.J., 2001, *ApJ*, 554, 803

This paper has been typeset from a \TeX/L\AA\TeX file prepared by the author.